The Journal of Chemical Physics

RESEARCH ARTICLE | OCTOBER 29 2026

Hybrid mechanics of coupled qubits

Merfat Alzomai ; Dmitrii V. Shalashilin

Check for updates

J. Chem. Phys. 165, 164130 (2026)
https://doi.org/10.1063/5.0349433

View Online
Export Citation

12 November 2026 10:25:53

AIP Publishing
The Journal of Chemical Physics
Special Topics Open for Submissions
Learn More

AIP Publishing

The Journal of Chemical Physics ARTICLE pubs.aip.org/aip/jcp

Hybrid mechanics of coupled qubits

Cite as: J. Chem. Phys. 165, 164130 (2026); doi: 10.1063/5.0349433
Submitted: 23 June 2026 • Accepted: 8 October 2026 •
Published Online: 29 October 2026

View Online Export Citation CrossMark

Merfat Alzomai[1,2,3,a] and Dmitrii V. Shalashilin[3,b]

AFFILIATIONS

[1] Department of Physics, College of Science, Imam Muhammad Ibn Saud Islamic University (IMSIU), Riyadh, Saudi Arabia
[2] School of Physics and Astronomy, University of Leeds, Leeds LS2 9JT, United Kingdom
[3] School of Chemistry, University of Leeds, Leeds LS2 9JT, United Kingdom

[a] mazumia2020@gmail.com
[b] Author to whom correspondence should be addressed: d.shalashilin@leeds.ac.uk

ABSTRACT

We find that a technique analogous to hybrid mechanics previously developed for Gaussian coherent states and molecular vibrations, can be extended to SU(2) coherent states describing coupled qubits. This formulation reveals a sparse structure of the propagator, leading to a computationally efficient scheme while maintaining numerical accuracy. As a result, the method enables simulations of larger qubit systems on classical computers. In particular, we demonstrate accurate real-time propagation for systems of up to 21 qubits, which would be computationally demanding using straightforward quantum-dynamics approaches.

© 2026 Author(s). All article content, except where otherwise noted, is licensed under a Creative Commons Attribution (CC BY) license (https://creativecommons.org/licenses/by/4.0/). https://doi.org/10.1063/5.0349433

12 November 2026 10:25:53

I. INTRODUCTION

In this paper, we generalize hybrid mechanics (HM), originally developed for Gaussian coherent states of the harmonic oscillator, to SU(2) coherent states describing coupled qubits. Simulating the real-time dynamics of quantum many-body systems remains a central challenge due to the exponential growth of the Hilbert space, which scales as 2^N for an N-qubit system. To address this challenge, we develop an efficient coherent-state framework for large-scale many-body dynamics based on SU(2)-HM. Exponential growth of the basis set renders brute-force methods infeasible and limits access to strongly interacting, nonperturbative, and out-of-equilibrium regime.[1–4] Even advanced tensor-network approaches, including matrix product states, MPS time-evolution methods, and entanglement-restricted techniques, lose efficiency when entanglement spreads rapidly, as commonly occurs in nonintegrable quenches and quantum-chaotic dynamics.[4–6] More expressive frameworks, such as neural-network-assisted tensor networks[7] and hybrid tensor-network ansätze,[8] exhibit similar limitations, reflecting a broader conceptual observation: although the Hilbert space grows exponentially, the dynamically explored region is often substantially smaller.

A growing body of theoretical and experimental work suggests that many-body quantum evolution frequently unfolds within emergent low-dimensional manifolds shaped by semiclassical structure, approximate conservation laws, and sparsity in effective propagators.[9–11] The concept of quantum scars was originally introduced in the semiclassical theory of quantum chaos as quantum states associated with unstable periodic classical trajectories embedded within a large phase-space manifold.[12–15] The term has since been generalized to describe long-lived metastable quantum states that persist within a dense spectrum of many-body states. Quantum many-body scars provide an important example: certain initial states exhibit long-time regular dynamics resembling metastable classical periodic trajectories confined to measure-zero regions of Hilbert space while exhibiting anomalously slow entanglement growth despite underlying nonintegrability.[11,13–15] This behavior suggests that large-scale qubit dynamics may admit efficient coherent-state representations when expressed in appropriate phase-space coordinates. Coherent states provide a natural framework for describing such semiclassical phase-space structure, forming localized wave packets that bridge classical trajectories and quantum many-body dynamics.

Several semiclassical methods based on Gaussian coherent states have been developed for simulations of quantum vibrational degrees of freedom. Gaussian coherent states are localized minimum-uncertainty wave packets in phase space, typically represented as Gaussian functions in position space with well-defined

© Author(s) 2026

centers in position and momentum. They are based on the frozen Gaussian approximation, which assumes that an ensemble of Gaussian coherent states guided by classical trajectories describes accurately short-time dynamics of coupled oscillators, such as vibrational modes of a molecule. In the frozen Gaussian approach, the width of each Gaussian wave packet is kept fixed during propagation, while only its center evolves in time. For harmonic oscillator systems, trajectory-guided Gaussian coherent states provide an exact solution of the time-dependent Schrödinger equation (TDSE). For anharmonic systems, a small basis of trajectory-guided Gaussian CSs typically provides accurate solutions for short times. Even a single trajectory-guided frozen Gaussian can provide an accurate short-time solution of the TDSE for systems of many coupled oscillators. The guiding trajectories may be obtained from a fully variational formulation, in which all wave-function parameters are coupled [16,17] or, more conveniently, approximated by classical or near-classical trajectories, as in the coupled coherent states (CCS) method.[18] These ideas have led to the development of a range of methods for simulating molecular dynamics and chemical processes.[19,20]

Since semiclassical and trajectory-based methods in many-body systems are typically limited to short-time dynamics, a framework combining trajectory-guided propagation with quantum evolution on a static grid of coherent states (CSs) was introduced under the name hybrid mechanics (HM),[21] as illustrated in Fig. 1. In the simplest form of HM, each element of a regular grid of Gaussian CSs is selected and propagated semiclassically along its trajectory. During this propagation, it accumulates a quantum phase. The end point CS is then projected onto basis coherent states, yielding a column of the propagator. Propagator matrix is sparse because only neighboring CSs with large overlap with the end point contribute to reprojection. The practical applicability of HM to Gaussian coherent states remained limited because large Gaussian coherent-state grids are required even for low-dimensional systems. For example, HM has been applied to the description of high harmonic generation[22] but for a 1D model only.

It has been shown that many ideas developed for Gaussian CSs can be generalized to other types of CSs.[23–27] This motivates the extension of HM to SU(2) coherent states, which naturally describe two-level systems and provide a phase-space representation for coupled qubit dynamics. In the present work, we demonstrate that hybrid mechanics originally developed to treat molecular vibrations provides an efficient framework for quantum propagation in coupled spin (qubit) systems by revealing and exploiting sparsity in the quantum propagator. Importantly, the resulting formulation preserves the essential dynamical features while substantially reducing computational cost.

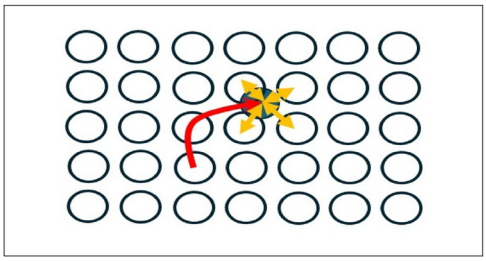


FIG. 1. Schematic illustration of hybrid mechanics (HM). The red arrow represents the trajectory of the initial coherent state, and the orange arrows indicate reprojections of the end point CS (red) onto neighboring CSs.

Direct SU(2)-CCS propagation becomes computationally demanding for large basis sets due to dense overlap and Hamiltonian matrices, which scale as $O(M^2)$, a square of the basis set size.[18,20,28] In contrast to tensor-network and related entanglement-based approaches,[3,5,16] the present formulation exploits the intrinsic coherent-state locality of SU(2) coherent states.[10,29,30] The resulting sparsity reflects the geometric structure of qubit phase space rather than externally imposed truncation. It enables accurate dynamics within compact dynamical subspaces, consistent with constrained many-body systems and quantum scar studies.[11,13,14,31]

While the proposed approach achieves good accuracy and computational efficiency by exploiting sparsity in the coherent-state representation, its performance depends on the identification of dynamically relevant subspaces and may require careful selection of basis parameters for highly delocalized states. Motivated by these considerations, we introduce a scalable two-stage SU(2)-HM framework tailored for large multi-qubit Hamiltonians. In the first stage, the Rydberg Hamiltonian introduced in Ref. 32 is represented in a static zero-contact SU(2) coherent-state basis related to the constrained Hilbert-space description developed for Rydberg-blockaded systems by Turner *et al.*[13] and later employed for multi-qubit sampling by Chuang and Pendse.[26] This basis is employed to construct a dense reference representation and identify the sparsity pattern of the short-time propagator. In the second stage, this structure is used to construct a sparse HM propagator, U_{sparse}, stored efficiently in the coordinate-list COO sparse matrix format while retaining all physically relevant couplings. Benchmark simulations for systems of 7 and 16 qubits demonstrate that sparse SU(2)-HM reproduces the reference autocorrelation and cross correlation functions with good agreement. The accuracy of the sparse propagation is controlled primarily by the sparsification threshold, although the quality of the semiclassical approximation may deteriorate for long propagation times. Memory usage and runtime are substantially reduced. While static calculations using the full basis remained computationally feasible only up to nine qubits, the zero-contact basis extended static simulations to 16 qubits. Dynamical propagation using the full-matrix representation within the zero-contact basis remained feasible up to 16 qubits, while the sparse HM propagator enabled dynamical simulations for systems of up to 21 qubits on a single CPU machine.

These results establish sparse SU(2)-HM as a practical and accurate framework for real-time evolution in many-body qubit systems and highlight the presence of compact coherent-state manifolds that can be identified and exploited to overcome scaling barriers in classical simulation. The present framework provides a route toward scalable simulations of larger quantum systems and may facilitate the study of non-equilibrium dynamics, quantum information processing, and emergent semiclassical structures in complex many-body systems.

12 November 2026 10:25:53

© Author(s) 2026

II. THEORY

A. Benchmark model, zero contact basis, and initial state

As a benchmark model, we consider an interacting Rydberg-qubit Hamiltonian with long-range van der Waals interactions,

$$\hat{H} = \frac{\Omega}{2}\sum_{i=1}^{N} \sigma_i^x - \Delta\sum_{i=1}^{N} n_i + \sum_{i<j} V_{ij}\, n_i n_j \tag{1}$$

The Hamiltonian follows the standard Rydberg-atom formulation of the Ref. 32. Here, Ω is the Rabi frequency governing coherent driving between qubit states and Δ is the detuning. The first term describes coherent spin-flip processes; the second term corresponds to on-site energy shifts; and the third term describes long-range van der Waals interactions between excited qubits. For atoms in Rydberg states, their interaction strength decreases with the distance R_{ij} between qubits i and j as

$$V_{ij} \propto \frac{1}{R_{ij}^6}, \tag{2}$$

where V_{ij} is the van der Waals interaction strength between atoms i and j. In Eq. (1),

$$\sigma_i^x = |0\rangle_i\langle 1| \; + |1\rangle_i\langle 0| \tag{3}$$

denotes the spin-flip operator acting on qubit i, while $n_i = |1\rangle_i\langle 1|$ is the excitation-number operator. Throughout this work, $\hbar = 1$ is assumed. Following the standard Rydberg-atom Hamiltonian formulation of Bernien *et al.*,[11] all Hamiltonian parameters are expressed in frequency units (MHz). Consequently, Ω, Δ, and V_{ij} all have units of MHz. The parameters are chosen as $\Omega = 2\pi$ and $\Delta = 0$, while the interaction strength is given by

$$V_{ij} = \frac{24\pi}{|i-j|^6}, \tag{4}$$

where $|i-j|$ denotes the separation between qubits measured in lattice sites. Consequently, time is measured in units of $1/\Omega$. Since the energy scale is expressed in MHz and $\hbar = 1$, the corresponding natural unit of time is $1/\text{MHz} = 10^{-6}$ s, i.e., microseconds (μs). No nearest-neighbor approximation is employed. All pairwise interactions $i < j$ are retained in the Hamiltonian, such that the full long-range van der Waals coupling is included. This is physically relevant because Rydberg interactions decay as R^{-6} rather than vanishing beyond nearest neighbors. Although distant interactions are weaker, they still contribute to collective many-body dynamics and may influence coherent oscillations, blockade effects, and the structure of dynamically relevant subspaces. However, as the interaction V_{ij} decreases sharply with $|i-j|$, the basis functions with no excitation of the neighboring qubits are lower in energy and are separated from other basis functions by a significant energy gap. For example, the energy of the state $|01010\ldots\rangle$ is lower than that of the state $|11010\ldots\rangle$. The former state $|01010\ldots\rangle$ belongs to the so-called zero contact basis, $\{Z_k^0\}_{k=1}^{M_0}$, defined as the set of basis states containing no neighboring excitations. The size M_0 of the zero contact basis still grows exponentially with the number of qubits N but much more slowly than the full Hilbert-space dimension 2^N.

The dynamics are initiated from selected product-state configurations belonging to the zero-contact manifold. These states are chosen as representative initial conditions for probing coherent many-body dynamics within the constrained Hilbert-space sector. The Hamiltonian provides a quantitative description of experimentally relevant Rydberg systems[11,33,34] and exhibits nontrivial many-body dynamics, which we aim to reproduce in our numerical simulations.

B. SU(2) spin-1/2 coherent states and short-time propagator

One-directional Gaussian coherent states are labeled by a single complex number z and expressed as a superposition of harmonic-oscillator quantum states,

$$|z\rangle = \sum_{n=0,\ldots,\infty} \frac{z^n}{\sqrt{n!}} e^{-\frac{|z|^2}{2}} |n\rangle. \tag{5}$$

Here, $|n\rangle$ denotes the nth harmonic-oscillator eigenstate. Gaussian coherent states correspond to minimum-uncertainty wave packets in the harmonic oscillator Hilbert space and are commonly used to describe semiclassical dynamics in systems with continuous degrees of freedom.[12,29,35] Although the present work focuses on qubit systems, Gaussian coherent states are introduced here as a reference framework since the HM technique was originally developed in the context of coupled oscillator systems.

In Eq. (5), $z = \frac{\gamma^{1/2}q + i\gamma^{-1/2}\hbar^{-1}p}{2^{1/2}}$ is a complex number describing a phase-space point of the harmonic oscillator and including the coordinate q, momentum p, and width γ of the Gaussian wave packet $\langle x|z\rangle$ in coordinate representation. Since each qubit has only two quantum states, its SU(2) coherent state can be represented as

$$|z\rangle = \frac{1}{\sqrt{1+|z|^2}} \left(|0\rangle + z|1\rangle\right) = a_0|0\rangle + a_1|1\rangle. \tag{6}$$

Here, $z \in \mathbb{C}$ denotes a stereographic coordinate on the SU(2) manifold, representing a point on the Bloch sphere that serves as the SU(2) analog of a harmonic oscillator phase-space point.

The SU(2) coherent state introduced in Eq. (6) is closely related to the atomic coherent state used in descriptions of many-body bosonic Josephson junctions. The latter is also referred to as an SU(2), Bloch, or angular-momentum coherent state.[36] In a two-mode bosonic system with a fixed total number of particles, N, the atomic coherent state represents the collective many-body system within an SU(2) representation, whereas Eq. (6) corresponds to the spin-1/2 representation appropriate to a single two-level system. Thus, both states belong to the same general family of SU(2) coherent states, but correspond to different representations and physical realizations.

In mapping the Hamiltonian approach, Gaussian coherent states have been used for description of electronic states, modeling them by low vibrational states of harmonic oscillator.[12,37] In a two-level system, the two lowest states $v = 0$ and $v = 1$ would model the two-level system. Then, the wave function is propagated using a semiclassical Herman–Kluk propagator with the help of an ensemble of Gaussian CSs.[38] However, Gaussian CSs include all vibrational states, not just $v = 0, 1$, therefore, taking the dynamics outside of

12 November 2026 10:25:53

© Author(s) 2026

the Hilbert space. Using SU(2) CSs seems more consistent with the nature of the dynamics of qubits.

For an N-qubit system, the coherent-state basis is constructed as a direct product,

$$|Z\rangle = \bigotimes_{n=1}^{N} |z_n\rangle, \quad Z = (z_1, \ldots, z_N). \tag{7}$$

This representation preserves the native SU(2) geometry of two-level systems. It, therefore, provides a natural phase-space description of multi-qubit dynamics. In contrast to Gaussian coherent states, SU(2) coherent states encode the compact geometry of spin degrees of freedom and, therefore, offer a natural coherent-state manifold for qubit evolution.

Parameterizations of the qubit wavefunction other than Eq. (6) are also possible. For example, an SU(2) coherent state may also be expressed as a superposition of two qubit basis states. In the present work, we parameterize the SU(2) coherent state using two complex amplitudes, a_1 and a_0, satisfying the normalization constraint $|a_1|^2 + |a_0|^2 = 1$, where

$$a_1 = \frac{z}{\sqrt{(1+zz^*)}}, \quad a_0 = \frac{1}{\sqrt{(1+zz^*)}}. \tag{8}$$

The size of the complete basis set of an N-qubit system is 2^N. For the Hamiltonian considered in Eq. (1), configurations belonging to the so called zero-contact manifold are energetically separated from higher-contact configurations and form a smaller basis. Excitations that create neighboring qubit occupations are energetically suppressed, and the low-energy dynamics remain predominantly confined within the zero-contact sector of the Hilbert space.

As a test of SU(2)-HM, our objective in this paper will be to reproduce long-time coherent motion, such as beatings between the states $|10101\ldots\rangle$ and $|01010\ldots\rangle$ in which either even or odd qubits are initially excited. These long-time beatings are observed only for these specific initial conditions and characteristic of quantum scars. All other initial states decay rapidly.

Reproducing such long-lived coherent behavior presents a challenge for the numerical simulation of quantum dynamics. To achieve this, we employ hybrid mechanics (HM) and first generate a fixed set of coherent states $\{Z_k^0\}_{k=1}^{M_0}$ using the zero-contact rule.[13,39] The full Hilbert space is truncated, but the chosen coherent-state manifold provides an efficient representation of dynamically relevant configurations.[26] By construction, this basis is time-independent and defines a static coherent-state manifold that captures the dominant semiclassical structure of the dynamics. Using the static zero-contact basis set $\{|Z_k^0\rangle\}_{k=1}^{M_0}$, the short-time propagator is constructed. Each basis state $|Z_k^0\rangle = |Z_k^0(0)\rangle$ is propagated over a single time interval Δt according to the SU(2) coherent-state equations of motion [supplementary material A; Eq. (A.3)]. The coherent-state trajectories are integrated using a fourth-order Runge–Kutta (RK4) time step of $dt = 0.001$. The short-time propagator is constructed over an interval $\Delta t = 21dt = 0.021\ \mu$s. Thus, the propagator time step is 21 times larger than the trajectory integration time step, $dt = 0.001\ \mu$s, substantially reducing the number of propagation steps required for long-time dynamics. The propagated state $|Z_k(\Delta t)\rangle$ together with the associated action phase, $S_k(\Delta t)$, is then projected back onto the static basis, yielding the matrix elements of the short-time propagator,

$$U_{ik} = \left\langle Z_i^0(0) \mid e^{-i\hat{H}\Delta t} \mid Z_k^0(0) \right\rangle = \left\langle Z_i^0(0) \mid Z_k^0(\Delta t) \right\rangle e^{iS_k(\Delta t)}. \tag{9}$$

A trajectory-guided function $|Z_k^0(\Delta t)\rangle$ may evolve outside the region covered by the zero-contact basis. In Eq. (9), the propagated state is, therefore, reprojected onto the relevant zero-contact manifold $|Z_k^0(0)\rangle$.

The propagator is further symmetrized according to

$$U_{ij} = \left(\left(e^{-i\hat{H}\Delta t}\right)_{ij} \left(e^{-i\hat{H}\Delta t}\right)^*_{ji} \right)^{\frac{1}{2}}. \tag{10}$$

Repeating this procedure for all basis states k generates the full short-time propagator $U_{\text{full}} \in \mathbb{C}^{M_0 \times M_0}$, which advances the vector of the wave function zero-contact basis amplitudes according to

$$C(t + \Delta t) = U_{\text{full}}\, C(t), \tag{11}$$

where C is the vector of the amplitudes in the wave function expansion $|\Psi(t)\rangle = C_k(t)\ |Z_k^0\rangle$ in the chosen basis (static zero-contact basis in this case). Most of the elements of U_{full} are small in magnitude. To exploit this, a sparse propagator is constructed by applying a thresholding criterion to the full propagator,

$$|\, U_{ij}\, | < \varepsilon \Rightarrow U_{ij} = 0, \quad \varepsilon = 10^{-3}. \tag{12}$$

The resulting operator U_{sparse} retains only dynamically relevant couplings and is stored in the coordinate-list (COO) sparse matrix format, where each nonzero element is specified by its row index, column index, and value. This format explicitly stores only nonzero matrix elements, thereby minimizing memory usage and enabling efficient sparse matrix–vector multiplication. This behavior is consistent with a broader body of work, showing that many-body quantum dynamics often remain confined to restricted subspaces when expressed in physically adapted representations,[40] including tensor-network approaches[4,5] and studies of quantum many-body scars.[13,31] Here, however, the relevant submanifold emerges directly from the SU(2) semiclassical geometry itself, providing a physically transparent foundation for the sparse-propagator construction introduced in the second stage. A more detailed derivation of the short-time propagator based on the coupled coherent states equations of motion is provided in supplementary material A; see Eqs.(A.3) and (A.5)

C. Long-time propagation with sparse propagator

Long-time wavefunction dynamics are then propagated according to

$$C(t + n\ \Delta t) = (U_{\text{sparse}})^n C(0) \tag{13}$$

at negligible marginal computational cost per time step. Time evolution is performed using the thresholded propagator, U_{sparse}, constructed according to the sparsification criterion of Eq. (12) described above and in supplementary material A for more details. It is important that time step Δt is much bigger than the time step dt for propagating trajectory or the time step required for straightforward quantum propagation with static basis, which leads to significant saving of CPU time.

12 November 2026 10:25:53

© Author(s) 2026

It is important to distinguish the sparsity of the short-time propagator from localization of the evolving wavefunction. In the present implementation, the short-time propagator $U(\Delta t)$ is constructed and sparsified using a fixed threshold before the long-time propagation, and the resulting sparse matrix is subsequently reused at every propagation step. The sparsity pattern is, therefore, determined by the matrix elements of $U(\Delta t)$ in the chosen zero-contact SU(2) coherent-state basis and does not evolve with the propagated state. Although the wavefunction may become increasingly delocalized and entangled during the dynamics, this changes the expansion coefficients of the state rather than the sparsity pattern of the precomputed propagator. Consequently, within the present time-independent Hamiltonian and fixed-Δt implementation, the propagator does not become progressively less sparse with propagation time.

This two-stage construction outlined above establishes a clear separation between physical insight and numerical acceleration. The first stage identifies a compact, physically meaningful coherent-state manifold using the static zero-contact basis, without introducing sparsification or additional numerical approximation. The second stage exploits the resulting coherent-state locality to construct a sparse propagator that enables scalable time evolution.

The threshold ε is selected through systematic convergence testing to minimize the number of retained matrix elements while preserving benchmark observables, most notably the norm, autocorrelation function (ACF), and cross correlation function (CCF). Smaller values of ε are found to yield systematically improved agreement with the full zero-contact calculations at increased computational cost, consistent with the controlled error scaling of the CCS representation. For $\varepsilon = 10^{-3}$, the sparse propagator reproduces the full zero-contact dynamics with good agreement while reducing memory usage and runtime by orders of magnitude.

Let M denote the number of coherent states in the static basis and p the fraction of nonzero matrix elements retained after sparsification ($p \approx 0.03$–0.07). The computational cost associated with the dense propagator scales approximately as $\mathcal{O}(M^3)$ due to a matrix-vector multiplication. In contrast, the sparse HM propagator scales as $\mathcal{O}(pM^3)$, leading to substantial computational savings for large basis sets, as p decreases with the number of qubits M; see Table II.

For the Hamiltonian and sparsification threshold considered here, significant matrix elements of the sparse propagator U_{sparse} were found to occur predominantly between basis functions differing by at most three spin flips. This observation makes it possible to avoid explicit construction of the full propagator U_{full}, thereby providing additional computational savings. The short-time propagator is already dominated by a relatively small number of significant matrix elements before sparsification is applied. The sparsification procedure, therefore, reveals and exploits an existing feature of the dynamics rather than introducing an artificial one. Thus, the reduction in computational cost and memory requirements arises from exploiting physically motivated locality in the SU(2) coherent-state representation rather than from uncontrolled numerical approximations.

III. RESULTS

First, for seven qubits, we solved time-dependent Schrödinger equation in its simplest form $iC = \hat{H}C$, where $\hat{H}$ is the matrix of the Hamiltonian and C is the vector of the basis function amplitudes in the expansion of the wave function in the chosen basis set, which is either 2^N or zero-contact basis sets. Hybrid mechanics was not used. For the seven-qubit system described by the Hamiltonian in Eq. (1), the full basis and the reduced zero-contact basis produce indistinguishable dynamical observables within numerical accuracy, including the norm, the autocorrelation function (ACF), and the cross correlation function (CCF), throughout the entire propagation window, as shown in Fig. 2. The deviation in the autocorrelation function (ACF) between the two representations remains below numerical precision,

$$\delta_{\mathrm{ACF}}(t) = |\langle \psi_{\mathrm{full}}(0)|\psi_{\mathrm{full}}(t)\rangle - \langle \psi_{0c}(0)|\psi_{0c}(t)\rangle|, \tag{14}$$

$$\delta_{\mathrm{ACF}}(t) < 10^{-12}.$$

While Eq. (14) quantifies the deviation in the ACF, Fig. 2 shows the corresponding ACF and CCF obtained with full and zero contact basis sets, which remain indistinguishable within numerical precision.

This agreement demonstrates that the wavefunction remains confined to the zero-contact basis, a narrow region of the SU(2) coherent-state manifold. Importantly, this behavior persists with increasing system size. As shown in Table I, the size of the zero-contact basis grows only modestly with N, remaining substantially smaller than the exponentially growing full Hilbert-space dimension 2^N. For example, at $N = 21$, the zero-contact basis contains only 28 657 states compared with 2 097 152 states in the full basis, corresponding to a reduction of 98.6%.

Then, we constructed HM propagator as described above. Table II illustrates the sparsity of the propagator within the zero-contact basis by comparing the total number of matrix elements in the nontruncated ($\varepsilon = \infty$) and truncated HM sparse propagators ($\varepsilon < 10^{-3}$) for different system sizes. Although the size of the zero-contact basis increases with N, the fraction of retained matrix elements decreases systematically, from 64.36% at $N = 7$ to only

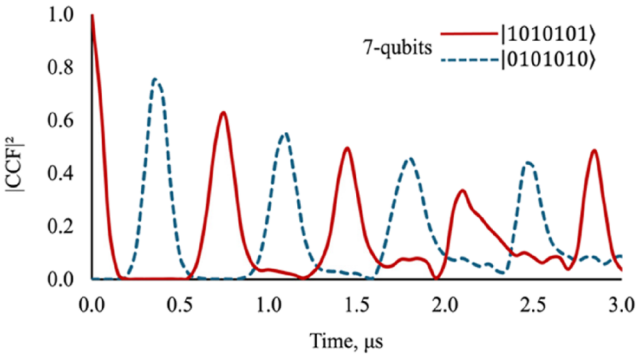


FIG. 2. Time evolution of the auto-correlation function and cross-correlation function (ACF and CCF) between the complementary product-state configurations $|1010101\rangle$ and $|0101010\rangle$, computed using the full HM basis and the reduced zero-contact basis. The results obtained with full and zero-contact basis sets are indistinguishable within numerical accuracy, indicating that the zero-contact basis captures the dynamically relevant SU(2)-HM subspace. Long-term recurrencies are the signature of quantum scars.

12 November 2026 10:25:53

© Author(s) 2026

TABLE I. Comparison of the full coherent-state basis and the reduced zero-contact basis for different system sizes N during the static stage. The reduction percentage indicates the decrease in basis size due to the zero-contact restriction.

N	Full basis	0-C basis	Reduction (%)
7	128	34	73.4
9	512	89	82.6
14	16 384	987	94.0
16	65 536	2584	96.1
18	262 144	6765	97.4
19	524 288	10 946	97.9
20	1 048 576	17 711	98.3
21	2 097 152	28 657	98.6

TABLE II. Sparsity of the propagator in the dynamic stage. Total and retained numbers of matrix elements in the full propagator U_{full} and sparse propagator U_{sparse} within the zero-contact basis for different system sizes N. The retained fraction denotes the percentage of matrix elements preserved after sparsification.

N	0-C basis	U_{full}	U_{sparse}	Retained (%)
7	34	1156	744	64.36
9	89	7921	3479	43.92
16	2584	6 677 056	432 882	6.48
18	6765	45 765 225	1 551 081	3.39
19	10 946	119 815 716	2 902 656	2.42
20	17 711	313 679 521	5 395 685	1.72
21	28 657	821 223 649	9 968 775	1.21

1.21% at $N = 21$. Consequently, HM dynamical propagation using the nontruncated-matrix representation within the zero-contact basis remained computationally feasible up to $N = 16$, whereas the truncated HM sparse propagator enabled simulations up to $N = 21$. This increasing sparsity provides the key numerical advantage that makes large-scale propagation computationally feasible.

To quantify the computational saving introduced by sparsification, we considered the 16-qubit system and varied the threshold over $\varepsilon = 10^{-1}, 10^{-2}, 10^{-3}, 10^{-4}, 10^{-9}$, and 10^{-10}. For each threshold, we determined the number and fraction of retained propagator elements and measured the computational cost of applying the resulting sparse propagator over 140 propagation steps. The results are summarized in Table III.

As shown in Table III, increasing the threshold progressively discards more propagator elements, reducing the number of retained non-zero elements (nnz) and consequently the computational cost of the sparse matrix–vector multiplication. The retained fraction decreases from 86% (5,725,800 elements) at $\varepsilon = 10^{-10}$ to 0.4% (26,228 elements) at $\varepsilon = 10^{-1}$. Correspondingly, the accumulated matrix–vector multiplication time decreases from 110.292 to 0.492 s, representing a ~224-fold reduction in the cost of the sparse propagation kernel.

The matrix–vector multiplication time scales approximately linearly with the number of retained propagator elements. Across the thresholds considered, the measured time per retained element per propagation step remains $\sim 1.3–1.4 \times 10^{-7}$ s, consistent with a $O(nnz)$ computational cost for the present COO sparse matrix–vector implementation. The reduction in the total propagation time is less pronounced because the full propagation loop also contains operations that are not directly reduced by sparsification, including the calculation of the norm and correlation functions and output operations.

The computational saving introduced by sparsification must be evaluated together with resulting propagation accuracy. At the two most aggressive sparsification thresholds, $\varepsilon = 10^{-1}$ and $\varepsilon = 10^{-2}$, the computational cost is substantially reduced; however, this reduction is accompanied by significant deviations of the average norm from unity, with values of 2.048 and 1.384, respectively. At $\varepsilon = 10^{-3}$, only 6.5% of the propagator elements are retained, and the matrix–vector multiplication time decreases from 110.292 s at $\varepsilon = 10^{-10}$ to 8.338 s, corresponding to a ~13.2-fold reduction in the sparse matrix–vector multiplication cost, while the average norm remains much closer to unity at 1.017. A less aggressive threshold of $\varepsilon = 10^{-4}$ further improves the norm conservation, giving an average norm of 0.998, although the matrix–vector multiplication time increases to 19.594 s. These results demonstrate a clear accuracy–cost trade-off: increasing the degree of sparsification reduces the computational cost, but excessively aggressive sparsification leads to a loss of propagation accuracy, whereas retaining more propagator elements improves accuracy at the expense of increased computational cost. Detailed timing and norm statistics for all six thresholds, together with the corresponding CCF dynamics, are provided in Table D1 and Fig. D1 of supplementary material D.

As shown in Fig. 3, the magnitude of propagator matrix elements decreases rapidly with increasing Hamming-distance ΔN between coherent-state configurations, i.e., the number of qubits

TABLE III. Dependence of the sparse-propagator computational cost on the sparsification threshold ε for the 16-qubit system ($n_{\text{basis}} = 2584$). The number and fraction of retained propagator elements are reported together with the accumulated sparse matrix–vector multiplication (matvec) time over 140 propagation steps and the corresponding average time per step.

ε	nnz	Retained (%)	Removed (%)	Matvec time (s)	Avg. matvec/step (s)
10^{-1}	26 228	0.3928	99.6072	0.492 454	0.003 518
10^{-2}	124 518	1.8649	98.1351	2.267 025	0.016 193
10^{-3}	432 882	6.4831	93.5169	8.337 632	0.059 555
10^{-4}	1 050 788	15.7373	84.2627	19.594 488	0.139 961
10^{-9}	5 247 680	78.5927	21.4073	100.548 420	0.718 203
10^{-10}	5 725 800	85.7534	14.2466	110.291 564	0.787 797

12 November 2026 10:25:53

© Author(s) 2026

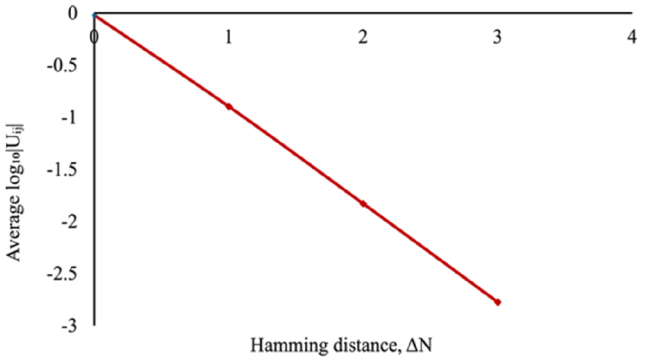


FIG. 3. Locality structure of the short-time propagator. Average values of $\log_{10}|U_{sparse}|$ as a function of the Hamming-distance ΔN between coherent-state basis configurations. The rapid decay of matrix-element magnitude with increasing ΔN indicates that dynamically relevant couplings occur only between states connected by a small number of local spin rotations.

different in two basis functions. Significant couplings are, therefore, restricted to basis states that differ by only a small number of local spins. This behavior reveals a pronounced locality structure in the short-time propagator.

As a direct consequence of propagator sparsification, substantial computational savings are achieved in the dynamical propagation stage Fig. 4 compares the computational cost of our HM with sparse truncated propagator to that of straightforward solution of TDSE using full basis of 2^N-dimensional qubit basis function. For the latter, the propagation was feasible for up to nine qubits, and for the former, we were able to simulate the system with up to 21 qubits using both serial and parallel versions of the code. Further details about computational cost and scaling are provided in the supplementary material.

The 21-qubit system represents the practical limit reached with the present implementation rather than a fundamental upper limit of the SU(2)-HM formulation. For $N = 21$, the zero-contact basis contains 28 657 states, corresponding to 8.21×10^8 possible

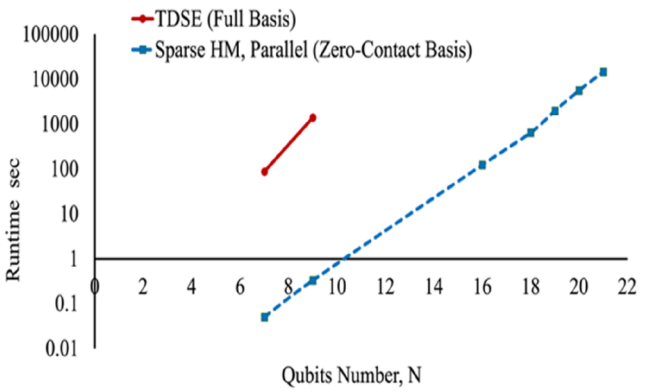


FIG. 4. Wall-clock time for dynamical SU(2)-HM propagation as a function of system size N using full 2^N basis and hybrid mechanics with zero contact basis and sparse propagator matrix.

propagator matrix elements. After application of the threshold $\varepsilon = 10^{-3}$, only 9.97×10^6 elements are retained, corresponding to 1.21% of the full propagator, as reported in Table II. While Table I shows that the zero-contact basis grows only moderately with N, the number of possible propagator matrix elements scales as the square of the basis size. Consequently, even this moderate growth in the basis leads to a much steeper increase in the computational cost of propagator construction. For $N = 22$, the zero-contact basis increases to 46 368 states, corresponding to $\sim 2.15 \times 10^9$ possible matrix elements, about 2.62 times the number for $N = 21$. In

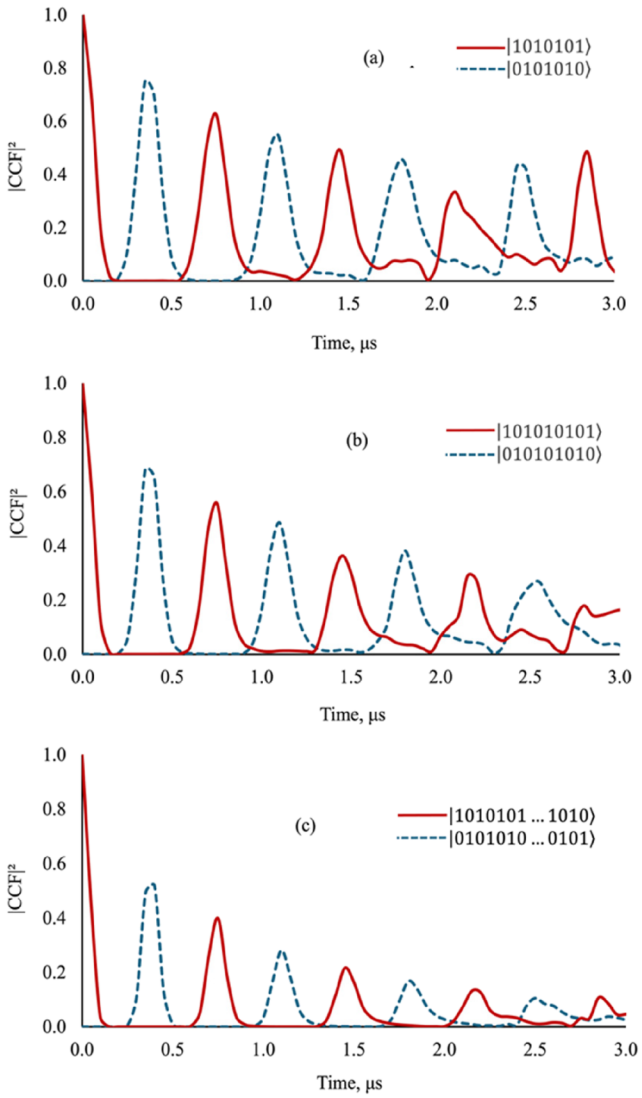


FIG. 5. Cross-correlation functions obtained from the straightforward solution of the TDSE in the static representation. Full-basis and zero-contact CCFs for increasing system sizes: (a) $N = 7$ qubits, (b) $N = 9$ qubits, and (c) zero-contact basis $N = 16$ qubits. For $N = 7$ and 9, the two curves coincide within numerical accuracy, confirming that the reduced zero-contact manifold reproduces the relevant dynamical correlations. For $N = 16$, the full 2^N basis becomes computationally impractical and only the zero-contact basis calculation is feasible.

12 November 2026 10:25:53

© Author(s) 2026

our attempted $N = 22$ calculation, construction of the short-time propagator could not be completed within the maximum 48-h wall time allowed for a single computational job. Thus, although the retained fraction decreases with increasing system size, the computational cost of the propagator-construction stage continues to increase. Extension beyond 21 qubits will, therefore, require further optimization of the propagator construction, greater computational resources, or both.

Figure 5 shows the cross correlation functions (CCFs) between the selected initial product-state configurations $|1010\ldots\rangle$ and $|0101\ldots\rangle$ for different system sizes. The observed decaying recurrences are consistent with signatures commonly associated with quantum many-body scar dynamics.

Furthermore, the sparse propagator significantly extends the accessible system size, enabling simulations up to 21 qubits without parallelization and within standard memory constraints. Parallelization was also used improving the performance of HM even further; see supplementary material B for more details.

Figure 6, therefore, examines the cross correlation function (CCF) during dynamical propagation within the zero-contact basis and sparse propagator, i.e., using hybrid mechanics. The sparse propagator is constructed using the thresholding condition $\varepsilon = 10^{-3}$, which removes dynamically negligible matrix elements and substantially reduces the size of the propagation operator.

Figure 6 shows that for $N = 7, 9$ and $N = 16$, where both full-matrix and sparse propagation remain computationally feasible, the CCFs obtained with the sparse HM propagator remain in agreement with the corresponding full-matrix results despite the substantial reduction in propagator size. Only the decay of correlation functions with time becomes faster when a sparce propagator is used. The deviations arise from the thresholding procedure introduced during sparsification and approximate nature of the semiclassical short time propagator (9, 10). Nevertheless, the dominant oscillatory structure and coherent beating dynamics are preserved, indicating that the essential correlation dynamics are accurately captured. Importantly, no irreversible decay or collapse of the oscillatory structure is observed for any system size considered, indicating the absence of dynamical instability or uncontrolled dephasing over the simulated time window. HM propagation within the zero-contact basis enabled simulations up to 21 qubits. Even for the largest system size considered, the characteristic oscillatory structure remains clearly resolved, demonstrating that the sparse propagator retains the relevant dynamical behavior while substantially extending the accessible system size.

To further assess convergence with respect to the sparsification threshold, additional calculations were performed for the $N = 7$ system using several values of ε. The resulting correlation functions were compared with an effectively non-truncated reference

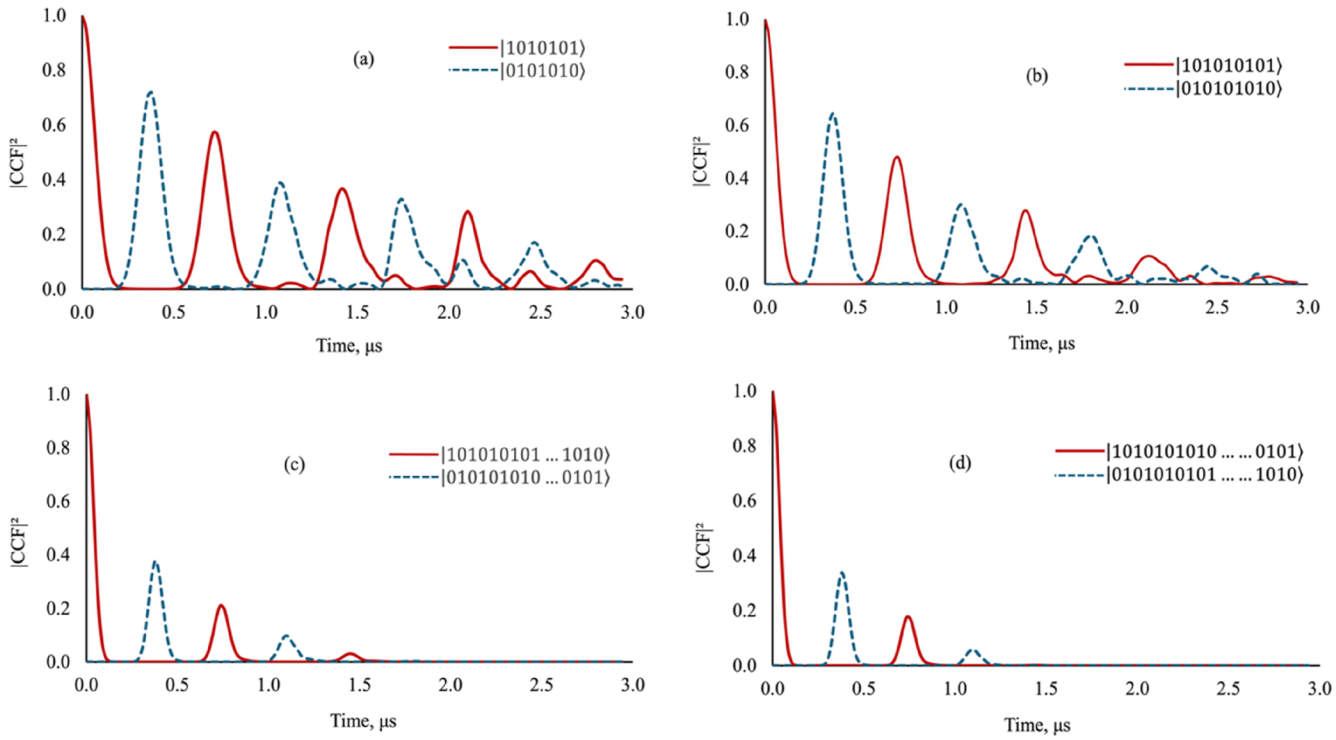


FIG. 6. Cross-correlation functions obtained by sparse HM dynamical propagation. CCFs computed using the sparse propagator U_{sparse} for increasing system sizes: (a) $N = 7$ qubits, (b) $N = 9$ qubits, (c) $N = 16$ qubits, and (d) $N = 21$ qubits. Oscillatory signatures remain observable for all system sizes, while the oscillation amplitude decreases gradually with increasing N.

12 November 2026 10:25:53

© Author(s) 2026

calculation using $\varepsilon = 10^{-10}$. As the threshold is reduced, the sparse results systematically approach the reference calculation. The corresponding threshold dependence of the CCF is shown in supplementary material C, Fig. C1, while the number and fraction of retained propagator matrix elements and the associated computational times are reported in supplementary material C, Table C1.

Due to the approximate nature of the thresholded propagator, norm conservation is not maintained to machine precision when sparse propagation is employed. The CCFs shown in Fig. 6 were, therefore, renormalized. The deviation from exact norm conservation provides a practical measure of the approximation introduced by the HM propagator and may be systematically reduced by decreasing the cutoff parameter ε, at the expense of additional computational cost.

IV. DISCUSSION AND CONCLUSIONS

The results presented above demonstrate that the sparse SU(2)-HM framework provides an accurate and computationally efficient description of many-body qubit dynamics for systems of up to 21 qubits. Nevertheless, several limitations and potential directions for further improvement remain. The present implementation employs a fixed time step and its behavior under adaptive or multiscale integration has not yet been explored. In addition, the sparsification threshold introduces an accuracy-efficiency trade-off that requires systematic characterization. Finally, the current formulation relies on a fixed zero-contact basis without adaptive refinement. This may limit efficiency when the evolving wavefunction explores regions of phase space insufficiently sampled by the initial coherent-state manifold. Although benchmark simulations reveal strong locality in coherent-state coupling ($\Delta N \leq 3$), this locality arises from the specific Hamiltonian structure and short-time propagation used here and its robustness across more general interaction models remains to be investigated.

The present SU(2)-HM construction is not specific to the Rydberg Hamiltonian. Since Ising and Heisenberg models are also formulated in terms of coupled spin degrees of freedom, they can be represented within an SU(2) coherent-state framework. Indeed, SU(2) spin-coherent-state representations have been employed in studies of both the Heisenberg model[41] and the transverse-field Ising model.[42] This suggests that the HM construction developed here could, in principle, be extended to other spin-1/2 Hamiltonians by constructing the corresponding short-time propagator on an appropriate SU(2) coherent-state basis. However, the strong locality and sparsity observed in the present calculations cannot be assumed to persist to the same degree for different Hamiltonians since the distribution of significant propagator matrix elements will depend on the structure and range of the spin interactions. The applicability, sparsity, and computational scaling of SU(2)-HM for Ising and Heisenberg models, therefore, remain to be investigated.

TDVP-MPS provides a natural alternative framework for the real-time dynamics considered here. In an MPS representation, the computational requirements depend strongly on the bond dimension χ, which controls the amount of entanglement that can be represented. The cost of standard MPS time-evolution algorithms increases polynomially with χ, with cubic dependence occurring in the dominant operations of commonly used implementations, while the scaling with the number of sites is generally favorable for one-dimensional systems. During real-time evolution, increasing entanglement may require a larger bond dimension to maintain a prescribed accuracy, thereby increasing the computational cost.[3,4,43] TDVP-MPS can also accommodate Hamiltonians with long-range interactions and, therefore, provides a relevant alternative for the Rydberg model considered here.[16,44]

In sparse SU(2)-HM, the computational control parameter and the origin of the accuracy–cost trade-off are different. Let M denote the size of the zero-contact coherent-state basis and p denote the fraction of propagator matrix elements retained after sparsification. Dense matrix–vector propagation scales approximately as $O(M^2)$, whereas the sparse matrix–vector multiplication scales as $O(nnz)$, where $nnz = pM^2$ is the number of retained propagator elements. This scaling is confirmed directly by the $N = 16$ hreshold analysis presented in Table III and supplementary material D, where the measured matrix–vector multiplication time varies approximately linearly with nnz. The approximation is controlled by sparsification of the short-time propagator using threshold ε, rather than by restricting the entanglement represented through an MPS bond dimension. The convergence analysis presented in supplementary material C, Fig. C1 shows that $\varepsilon = 10^{-3}$ provides substantial sparsification while preserving the principal correlation dynamics for the $N = 7$ benchmark. At this threshold, p decreases from 0.6436 for $N = 7$ to 0.0121 for $N = 21$, so that only 1.21% of the full zero-contact propagator is retained for the largest system considered. Thus, the computational reduction exploited here arises from the locality and sparsity of the propagator rather than from restricting the entanglement through an MPS bond dimension.

More general tensor-network geometries, such as tree tensor networks, provide alternative representations beyond the one-dimensional MPS structure and may be advantageous for different correlation and entanglement structures. Their efficiency, however, also depends on the required bond dimensions and the complexity of the associated tensor contractions.[45]

The potential advantage of sparse SU(2)-HM is, therefore, not the elimination of an accuracy–cost trade-off, but the introduction of a qualitatively different one governed by propagator sparsity. MPS methods are particularly effective when the dynamics can be represented with moderate bond dimensions, whereas sparse SU(2)-HM may be favorable when the short-time propagator remains strongly sparse in the chosen coherent-state basis. A quantitative comparison would require calculations performed at matched accuracy, propagation time, and computational conditions. Since such a benchmark has not been performed here, we regard sparse SU(2)-HM as a complementary approach and do not claim a its computational superiority.

Several directions for future work and further development can be suggested. Extending the framework to regimes where the wavefunction explores larger regions of phase space represents an important direction, potentially through adaptive refinement of the coherent-state manifold. Incorporating the observed $\Delta N \leq 3$ locality into propagator construction could further reduce matrix assembly and storage costs while preserving physically relevant couplings.

In the past few years, we have been developing a new approach to electronic structure theory and electron dynamics based on Bogolyubov states and Jordan–Wigner transformation, termed Zombie States.[28,46] Zombie States map a set of spin-orbitals to a set

12 November 2026 10:25:53

© Author(s) 2026

of qubits, and therefore, all techniques developed for coupled two-level systems, including hybrid mechanics, should be applicable to electronic structure and dynamics. Another useful direction could be combining HM with a Krylov-based method,[36,37] as Eq. (13) can clearly be used to generate Krylov space.

We have introduced a scalable SU(2)-hybrid mechanics framework for the simulation of many-body qubit dynamics. By exploiting the intrinsic geometric structure of SU(2) coherent states together with a sparsified short-time propagator, the method achieves orders-of-magnitude reductions in computational cost and memory requirements while reproducing reference observables. Benchmark simulations reveal strong locality in coherent-state coupling, with dynamically relevant interactions confined to a small Hamming-distance neighborhood ($\Delta N \leq 3$), providing a physical origin for propagator sparsity. The observed locality is already present in the unsparsified short-time propagator, indicating that sparsity emerges from Hamiltonian locality and the finite-order structure of short-time dynamics rather than from imposed truncation. The present generalization of hybrid mechanics, originally developed in chemical physics for molecular vibrational dynamics, provides a promising framework for scalable simulations of interacting many-body qubit systems while preserving the physically transparent structure of SU(2) coherent-state dynamics.

SUPPLEMENTARY MATERIAL

The supplementary material provides additional details of the computational implementation and numerical performance of the hybrid mechanics approach, including the construction and sparsification of the short-time propagator, computational scaling and timing data, parallelization results, and additional numerical results supporting the calculations presented in the main text.

ACKNOWLEDGMENTS

The authors acknowledge financial support from Imam Mohammad Ibn Saud Islamic University (IMSIU), Riyadh, Saudi Arabia. The authors thank Professors Zlatko Papić and Almut Beige for valuable discussions. The authors also acknowledge participation of Grace Hsiao-Han Chuang at the initial stage of the project. This research was funded through a studentship from Imam Mohammad Ibn Saud Islamic University (IMSIU), Riyadh, Saudi Arabia. This work was also supported by EPSRC under Grant No. EP/X026973/1.

AUTHOR DECLARATIONS

Conflict of Interest

The authors have no conflicts to disclose.

Author Contributions

Merfat Alzomai: Conceptualization (equal); Data curation (equal); Formal analysis (equal); Funding acquisition (equal); Methodology (equal); Software (equal); Writing – original draft (equal); Writing – review & editing (equal). **Dmitrii V. Shalashilin**: Conceptualization (equal); Funding acquisition (equal); Methodology (equal); Supervision (equal); Writing – original draft (equal); Writing – review & editing (equal).

DATA AVAILABILITY

The data supporting the findings of this study, including simulation codes and numerical results, are available from the corresponding author upon reasonable request.

REFERENCES

[1] M. A. Nielsen and I. L. Chuang, *Quantum Computation and Quantum Information* (Cambridge University Press, Cambridge, 2010).
[2] R. P. Feynman, "Simulating physics with computers," in *Feynman and Computation: Exploring the Limits of Computers*, edited by A. J. G. Hey (CRC Press, 2018), p. 133.
[3] U. Schollwöck, "The density-matrix renormalization group," Rev. Mod. Phys. **77**, 259 (2005).
[4] G. Vidal, "Efficient simulation of one-dimensional quantum many-body systems," Phys. Rev. Lett. **93**, 040502 (2004).
[5] S. R. White, "Density matrix formulation for quantum renormalization groups," Phys. Rev. Lett. **69**, 2863 (1992).
[6] J. Hauschild and F. Pollmann, "Efficient numerical simulations with tensor networks: Tensor network Python (TeNPy)," SciPost Phys. Lect. Notes, 5 (2018).
[7] K. Choo, G. Carleo, N. Regnault, and T. Neupert, "Symmetries and many-body excitations with neural-network quantum states," Phys. Rev. Lett. **121**(16), 167204 (2018).
[8] M. P. Zaletel and R. S. K. Mong, "Exact matrix product states for quantum Hall wave functions," Phys. Rev. B **86**, 245305 (2012).
[9] J. R. Klauder, "Path integrals and stationary-phase approximations," Phys. Rev. D **19**, 2349 (1979).
[10] W.-M. Zhang, D. H. Feng, and R. Gilmore, "Coherent states: Theory and some applications," Rev. Mod. Phys. **62**, 867 (1990).
[11] H. Bernien, S. Schwartz, A. Keesling, H. Levine, A. Omran, H. Pichler, S. Choi, A. S. Zibrov, M. Endres, M. Greiner *et al.*, "Probing many-body dynamics on a 51-atom quantum simulator," Nature **551**, 579 (2017).
[12] E. J. Heller, "Time-dependent approach to semiclassical dynamics," J. Chem. Phys. **62**, 1544 (1975).
[13] C. J. Turner, A. A. Michailidis, D. A. Abanin, M. Serbyn, and Z. Papić, "Weak ergodicity breaking from quantum many-body scars," Nat. Phys. **14**, 745 (2018).
[14] M. Serbyn, D. A. Abanin, and Z. Papić, "Quantum many-body scars and weak breaking of ergodicity," Nat. Phys. **17**, 675 (2021).
[15] W. W. Ho, S. Choi, H. Pichler, and M. D. Lukin, "Periodic orbits, entanglement, and quantum many-body scars in constrained models: Matrix product state approach," Phys. Rev. Lett. **122**, 040603 (2019).
[16] J. Haegeman, J. I. Cirac, T. J. Osborne, I. Pižorn, H. Verschelde, and F. Verstraete, "Time-dependent variational principle for quantum lattices," Phys. Rev. Lett. **107**, 070601 (2011).
[17] P. Kramer and M. Saraceno, *Geometry of the Time-dependent Variational Principle in Quantum Mechanics* (Springer, Berlin, 1981).
[18] D. V. Shalashilin and M. S. Child, "Description of tunneling with the help of coupled frozen Gaussians," J. Chem. Phys. **114**, 9296 (2001).
[19] D. V. Shalashilin and M. S. Child, "The phase space CCS approach to quantum and semiclassical molecular dynamics for high-dimensional systems," Chem. Phys. **304**, 103 (2004).
[20] D. V. Shalashilin, "Quantum mechanics with the basis set guided by Ehrenfest trajectories: Theory and application to spin-boson model," J. Chem. Phys. **130**, 244101 (2009).
[21] D. Huber and E. J. Heller, "Hybrid mechanics: A combination of classical and quantum mechanics," J. Chem. Phys. **89**, 4752 (1988).

12 November 2026 10:25:53

© Author(s) 2026

[22]C. Symonds, J. Wu, M. Ronto, C. Zagoya, C. Figueira de Morisson Faria, and D. V. Shalashilin, "Coupled-coherent-states approach for high-order harmonic generation," Phys. Rev. A **91**, 023427 (2015).
[23]M. A. Sepúlveda and F. Grossmann, "Time-dependent semiclassical mechanics," in *Advances in Chemical Physics* (John Wiley & Sons, 1996), Vol. 96, p. 191.
[24]A. O. Barut and L. Girardello, "New 'coherent' states associated with non-compact groups," Commun. Math. Phys. **21**, 41 (1971).
[25]Y. Qiao and F. Grossmann, "Revealing quantum effects in bosonic Josephson junctions: A multi-configuration atomic coherent state approach," Front. Phys. **11**, 1221614 (2023).
[26]H.-H. G. Chuang and A. Pendse, "Capturing spin chain dynamics with periodically projected time-dependent basis," arXiv:2306.07407 (2023).
[27]A. Grigolo, T. F. Viscondi, and M. A. M. de Aguiar, "Multiconfigurational quantum propagation with trajectory-guided generalized coherent states," J. Chem. Phys. **144**, 094106 (2016).
[28]D. V. Shalashilin and D. V. Makhov, "A new form of particle number conserving fermionic coherent states for electronic structure theory and electron dynamics," J. Chem. Phys. **163**, 131102 (2025).
[29]A. Perelomov, *Generalized Coherent States and Their Applications* (Springer-Verlag, Berlin, 1986).
[30]J. M. Radcliffe, "Some properties of coherent spin states," J. Phys. A: Gen. Phys. **4**, 313 (1971).
[31]S. Moudgalya, B. A. Bernevig, and N. Regnault, "Quantum many-body scars and Hilbert space fragmentation: A review of exact results," Rep. Prog. Phys. **85**, 086501 (2022).
[32]M. D. Lukin, M. Fleischhauer, R. Cote, L. M. Duan, D. Jaksch, J. I. Cirac, and P. Zoller, "Dipole blockade and quantum information processing in mesoscopic atomic ensembles," Phys. Rev. Lett. **87**, 037901 (2001).
[33]M. Saffman, "Quantum computing with atomic qubits and rydberg interactions: Progress and challenges," J. Phys. B: At., Mol. Opt. Phys. **49**, 202001 (2016).
[34]S. Ebadi, T. T. Wang, H. Levine, A. Keesling, G. Semeghini, A. Omran, D. Bluvstein, R. Samajdar, H. Pichler, W. W. Ho *et al.*, "Quantum phases of matter on a 256-atom programmable quantum simulator," Nature **595**, 227 (2021).
[35]E. J. Heller, "Frozen Gaussians: A very simple semiclassical approximation," J. Chem. Phys. **75**, 2923 (1981).
[36]S. Wimberger, G. Manganelli, A. Brollo, and L. Salasnich, "Finite-size eeffects in a bosonic Josephson junction," Phys. Rev. A **103**, 023326 (2021).
[37]W. H. Miller, "A classical analog for electronic degrees of freedom in nonadiabatic collision processes," J. Chem. Phys. **70**, 3214 (1979).
[38]M. F. Herman and E. Kluk, "A semiclassical justification for the use of non-spreading wavepackets in dynamics calculations," Chem. Phys. **91**, 27 (1984).
[39]I. Lesanovsky and H. Katsura, "Interacting fibonacci anyons in a Rydberg gas," Phys. Rev. A **86**, 041601 (2012).
[40]M. P. Zaletel, R. S. K. Mong, and F. Pollmann, "Topological characterization of fractional quantum Hall ground states from microscopic hamiltonians," Phys. Rev. Lett. **110**, 236801 (2013).
[41]J. Schliemann and F. G. Mertens, "Semiclassical description of Heisenberg models via spin-coherent states," J. Phys.: Condens. Matter **10**, 1091 (1998).
[42]R. Ng, E. S. Sørensen, and P. Deuar, "Simulation of the dynamics of many-body quantum spin systems using phase-space techniques," Phys. Rev. B **88**, 144304 (2013).
[43]S. Paeckel, T. Köhler, A. Swoboda, S. R. Manmana, U. Schollwöck, and C. Hubig, "Time-evolution methods for matrix-product states," Ann. Phys. **411**, 167998 (2019).
[44]J. Haegeman, C. Lubich, I. Oseledets, B. Vandereycken, and F. Verstraete, "Unifying time evolution and optimization with matrix product states," Phys. Rev. B **94**, 165116 (2016).
[45]P. Silvi, F. Tschirsich, M. Gerster, J. Jünemann, D. Jaschke, M. Rizzi, and S. Montangero, "The tensor networks anthology: Simulation techniques for many-body quantum lattice systems," SciPost Phys. Lect. Not., 8 (2019).
[46]O. A. Bramley, T. J. H. Hele, and D. V. Shalashilin, "Electronic energies from coupled fermionic 'Zombie' states' imaginary time evolution," J. Chem. Phys. **156**(17), 174116 (2022).
[47]D. V. Shalashilin, "Zombie states for description of structure and dynamics of multi-electron systems," J. Chem. Phys. **148**(19), 194109 (2018).

12 November 2026 10:25:53

© Author(s) 2026